Chinese Chemical Letters 34 (2023) 108246

Contents lists available at ScienceDirect

Chinese Chemical Letters

journal homepage: www.elsevier.com/locate/cclet

Boron doped 1T phase MoS_2 as a cocatalyst for promoting photocatalytic H_2 evolution of g-C_3N_4 nanosheets

Pengyuan Qiu[a,b,1], Yan An[a,1], Xinyu Wang[a], Shanna An[a], Xiaoli Zhang[c], Jian Tian[a,*], Wen Zhu[b,*]

[a] School of Materials Science and Engineering, Shandong University of Science and Technology, Qingdao 266590, China
[b] State Key Laboratory of Materials Processing and Die & Mould Technology, School of Materials Science and Engineering, Huazhong University of Science and Technology, Wuhan 430074, China
[c] School of Materials Science and Engineering, Zhengzhou University, Zhengzhou 450001, China

ARTICLE INFO

Article history:
Received 25 October 2022
Revised 5 February 2023
Accepted 17 February 2023
Available online 24 February 2023

Keywords:
1T phase MoS_2
g-C_3N_4 nanosheets
Photocatalytic H_2 evolution
Active sites
Boron doping

ABSTRACT

As one of the 2D transition metal sulfides, 1T phase MoS_2 nanosheets (NSs) have been studied because of their distinguished conductivity and suitable electronic structure. Nevertheless, the active sites are limited to a small number of edge sites only, while the basal plane is catalytically inert. Herein, we report that boron (B) doped 1T phase MoS_2 NSs can replace precious metals as a co-catalyst to assist in photocatalytic H_2 production of 2D layered g-C_3N_4 nanosheets (g-C_3N_4 NSs). The H_2 evolution rate of prepared B-MoS_2@g-C_3N_4 composites with 15 wt% B-MoS_2 (B-MoS_2@g-C_3N_4–15, 1612.75 μmol h^{-1} g^{-1}) is 52.33 times of pure g-C_3N_4 NSs (30.82 μmol h^{-1} g^{-1}). Furthermore, the apparent quantum efficiency (AQE) of B-MoS_2@g-C_3N_4–15 composites under the light at $\lambda = 370$ nm is calculated and reaches 5.54%. The excellent photocatalytic performance of B-MoS_2@g-C_3N_4–15 composites is attributed to the B ions doping inducing the distortion of 1T phase MoS_2 crystal, which can activate more base planes to offer more active sites for H_2 evolution reaction (HER). This work of B-MoS_2@g-C_3N_4 composites offers experience in the progress of effective and low-price photocatalysts for HER.

Recently, g-C_3N_4 nanosheets (NSs) have attracted much attention to hydrogen production due to excellent chemical stability, suitable band structure, simple syntheses, low cost and special two-dimensional (2D) layered structure [1–3]. Besides, the special nitrogen-rich polymeric structure of 2D layered g-C_3N_4 NSs could provide numerous active sites for HER [4,5]. Nevertheless, the photocatalytic hydrogen evolution performance of pure 2D layered g-C_3N_4 NSs is unsatisfactory because of fast electron-holes pairs recombination and insufficient absorption of light [6–8]. Hence, it is essential to exploit novel methods to enhance the H_2 generation performance of 2D layered g-C_3N_4 NSs. The construction of an internal electric field (IEF) is an effective strategy to enhance photocatalytic hydrogen evolution performance because of its key role in photo-induced carrier separation [9–11]. Precious metals act as cocatalysts is a common strategy to construct IEF [12,13]. Yet, the widespread application of precious metals is limited by high cost [14]. Hence, the development of an inexpensive and efficient co-catalyst is crucial for enhancing the photocatalytic activity of 2D layered g-C_3N_4 NSs.

Among various cocatalysts, transition-metal chalcogenides, such as MoS_2, receive widespread attention ascribed to the superior 2D layered structure [15–19]. MoS_2 has both semiconductor 2H phase and metallic 1T phase. Among them, metallic 1T phase MoS_2 NSs with octahedral coordination can improve the transfer and capture of photogenerated carriers to boost the photocatalytic H_2 evolution activity of 2D layered g-C_3N_4 NSs, attributing to excellent conductivity [20–22]. In addition, the Gibbs free energy of 1T phase MoS_2 NSs for H^+ absorption is near-zero, which is suitable for HER [6,23]. However, the basal plane of MoS_2 NSs is inert, which limits the photocatalytic hydrogen evolution reaction [6]. Recent researches show that MoS_2′s basal plane can be activated through doping atoms to design the active sites of MoS_2, attributed to the local electronic structure modulation [6,24–26]. Thus, boron (B) ions are incorporated into the lattice of 1T phase MoS_2 could activate the basal plane, which can improve photocatalytic H_2 production performance. Hence, 2D-layered g-C_3N_4 NSs modified by

* Corresponding authors.
E-mail addresses: jiantian@sdust.edu.cn (J. Tian), wennar@mail.hust.edu.cn (W. Zhu).
[1] These authors contributed equally to this work.

https://doi.org/10.1016/j.cclet.2023.108246
1001-8417/

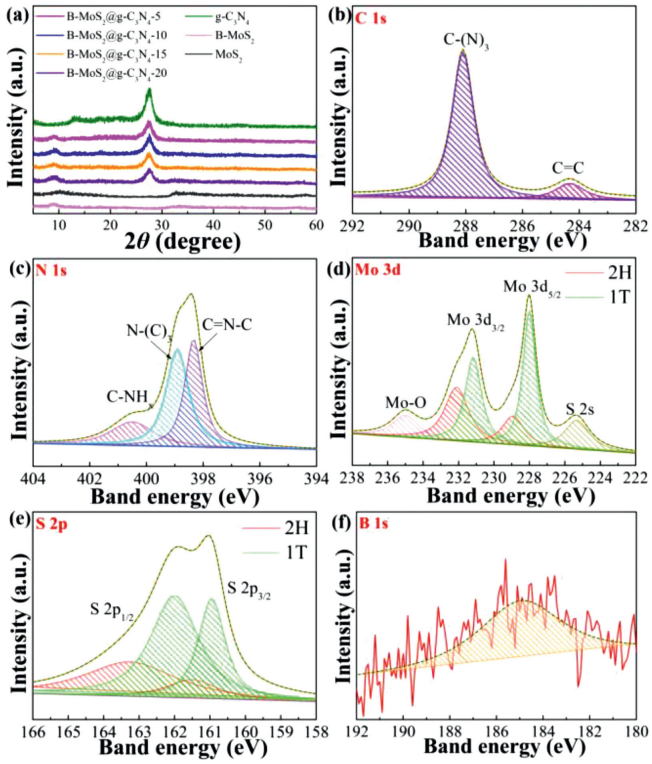

Fig. 1. (a) X-ray diffraction patterns of pure g-C_3N_4 NSs and B-MoS_2@g-C_3N_4 composites. (b) C 1s, (c) N 1s, (d) Mo 3d, (e) S 2p and (f) B 1s XPS spectra of B-MoS_2@g-C_3N_4–15 composites.

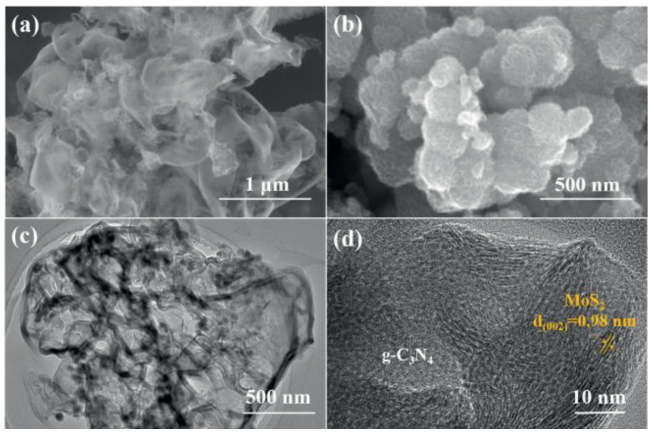

Fig. 2. SEM images of (a) pure g-C_3N_4 NSs and (b) B-MoS_2 NSs. (c) TEM and (d) HR-TEM images of B-MoS_2@g-C_3N_4–15 composites.

doping B into 1T phase MoS_2 NSs (B-MoS_2 NSs) could exhibit better photocatalytic performance.

In this work, we propose B-MoS_2@g-C_3N_4 composites for photocatalytic H_2 evolution, in which triethanolamine acts as the sacrificial agent. The B into 1T phase MoS_2 NSs are powerfully connected with 2D layered g-C_3N_4 NSs through an easy hydrothermal method. The synthesized B-MoS_2@g-C_3N_4 composites with 15 wt% B-MoS_2 (B-MoS_2@g-C_3N_4–15) display an efficient rate of hydrogen evolution (1612.75 μmol h^{-1} g^{-1}), which is 52.33 times as much as pure g-C_3N_4 NSs (30.82 μmol h^{-1} g^{-1}). In addition, the apparent quantum efficiency (AQE) of pure g-C_3N_4 NSs and B-MoS_2@g-C_3N_4–15 composites are 0.41 and 5.54% under the light at $\lambda = 370$ nm. The loading of B-MoS_2 NSs improves the light absorption of g-C_3N_4 to stimulate more photogenerated carriers. In addition, the incorporation of B ions into the lattice of 1T phase MoS_2 NSs can provide more active sites and speed up the photocatalytic hydrogen evolution reaction. Thus, B-MoS_2@g-C_3N_4 composites display excellent photocatalytic H_2 production activity.

The fabrication of B-MoS_2@g-C_3N_4 composites is displayed in Scheme S1 (Supporting information). Firstly, pure g-C_3N_4 NSs are synthesized *via* a direct thermal polymerization way of urea. During heating, urea first reacts to form bulk g-C_3N_4 when the muffle furnace temperature is kept at 550 °C, and then g-C_3N_4 NSs with 2D layered structure are formed at the muffle furnace temperature of 500 °C. Afterward, g-C_3N_4 NSs, ammonium tetrathiomolybdate and boric acid are added to the 70 mL *N*,*N*-dimethylformamide solution and evenly dispersed. Then, B-MoS_2 NSs are grown on the surface of g-C_3N_4 NSs by hydrothermal method to obtain B-MoS_2@g-C_3N_4 composites.

For pure g-C_3N_4 NSs and B-MoS_2@g-C_3N_4 composites, two characteristic peaks are located at 13.1° and 27.4° (green, pink, blue, yellow and purple curves in Fig. 1a), attributing to (100) and (002) planes of g-C_3N_4 (JCPDS No. 87–1526) [27–29]. Simultaneously, the peaks at 13.1° (100) and 27.4° (002) of g-C_3N_4 in B-MoS_2@g-C_3N_4 composites become weaker after B-MoS_2 NSs loading on g-C_3N_4 NSs, attributing to the fact that the order degree of g-C_3N_4 NSs is decreased by B-MoS_2 NSs incorporation [6]. As shown in black curve in Fig. 1a, there are two peaks at 10.2° and 32.5° indexed to (002) and (100) plane of MoS_2. Compared with pure MoS_2 (black curve in Fig. 1a), the peak at 10.2° of MoS_2 shifts to a lower degree of 8.8° in contrast to the 10.2° (002) peak of MoS_2 due to the B ions incorporating into the lattice of MoS_2 cause the distortion of MoS_2 crystal (red curve in Fig. 1a) [6]. In addition, the peak of B-MoS_2@g-C_3N_4 composites at 8.8° is similar to B-MoS_2, indicating that B-MoS_2 and g-C_3N_4 coexist.

To further analyze the chemical bonding state, the XPS spectra of B-MoS_2@g-C_3N_4 composites are tested. As shown in Fig. S1 (Supporting information), the survey XPS spectrum indicates that B-MoS_2@g-C_3N_4 composites consist of C, N, Mo, S and B. As shown in Fig. 1b, the C 1s XPS spectrum is deconvolved into two peaks at 284.8 and 288.4 eV, corresponding to C=C and C-$(N)_3$ bonds, respectively [30,31]. Fig. 1c indicates that the N 1s spectrum is deconvolved into three peaks at 398.2, 399.1 and 400.6 eV, attributing to C=N–C, N-$(C)_3$ and C–NH_x, respectively [32,33]. As shown in Fig. 1d, there are two green peaks at 227.8 and 230.9 eV, assigning to Mo $3d_{5/2}$ and Mo $3d_{3/2}$ of 1T phase [34]. The two pink peaks at 228.7 and 232.2 eV are attributed to Mo $3d_{5/2}$ and Mo $3d_{3/2}$ of 2H phase [34]. In addition, the peaks at 225.2 and 234.9 eV are assigned to S 2s and oxidation of Mo [6]. As for the S 2p XPS spectrum (Fig. 1e), two green peaks at 160.7 and 162.1 eV are attributed to S $2p_{3/2}$ and S $2p_{1/2}$ of 1T phase [35]. Simultaneously, there are two pink peaks at 161.5 and 163.4 eV, assigning to S $2p_{3/2}$ and S $2p_{1/2}$ of 2H phase [35]. Besides, according to Mo 3d and S 2p spectra, the proportion of 1T phase MoS_2 is about 71.2%, indicating that 1T phase MoS_2 in B-MoS_2@g-C_3N_4 composites is the main phase. Fig. 1f exhibits a visible peak of B element at 184.6 eV, illustrating the successful doping of B ions in MoS_2 [6]. Besides, the Raman spectrum of B-MoS_2 (Fig. S2 in Supporting information) is measured to determine the MoS_2 phase. There are three peaks at 147, 237, and 335 cm^{-1}, respectively, which correspond to the J_1, J_2, and J_3 modes of 1T phase MoS_2 [16].

As shown in Fig. 2a, g-C_3N_4 NSs display a special 2D layered structure, and the lamellae of g-C_3N_4 NSs present irregular wrinkled sheet morphologies. Pure B-MoS_2 displays flower-like assemblies composed of numerous small nanosheets (Fig. 2b). In Fig. 2c, B-MoS_2@g-C_3N_4 composites still keep typical 2D sheet-shaped morphology. As shown in Fig. 2d, B-MoS_2 NSs are assembled on the g-C_3N_4 NSs, and the lattice space distance (0.98 nm) is attributed to the (002) plane of MoS_2 [6]. The close connection be-

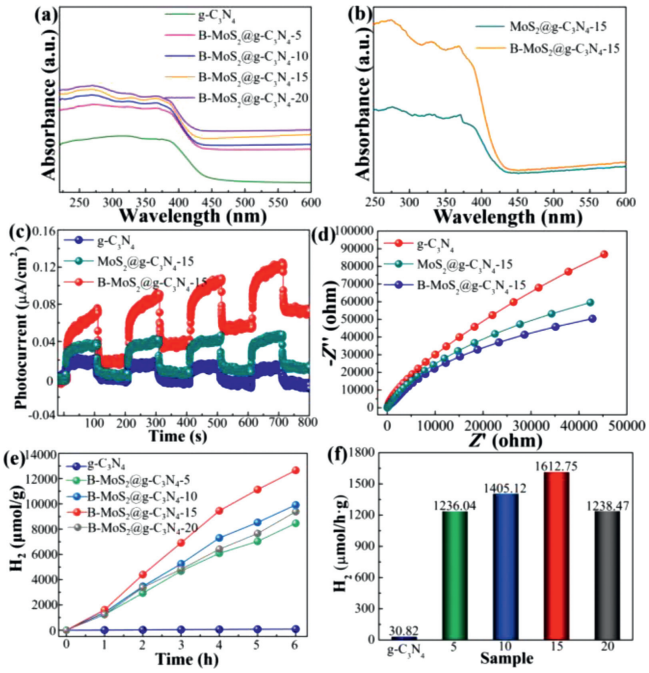

Fig. 3. (a) UV–vis DRS absorption spectra of g-C_3N_4 NSs and B-MoS_2@g-C_3N_4 composites. (b) UV–vis DRS absorption spectra of B-MoS_2@g-C_3N_4–15 and B-MoS_2@g-C_3N_4–15 composites. (c) Transient photocurrent responses. (d) EIS, (e) cumulated evolution and (f) photocatalytic H_2 production rates of the samples.

tween g-C_3N_4 NSs and B-MoS_2 NSs facilitates the fast transfer of photogenerated electrons from g-C_3N_4 NSs to B-MoS_2 NSs, which can effectively inhibit electron-hole pairs recombination. Fig. S3 (Supporting information) shows the EDX mapping images of B-MoS_2@g-C_3N_4–15 composites, which display even distribution of C, N, Mo, S and B, indicating the coexistence of g-C_3N_4 and B-MoS_2.

As shown in Fig. 3a, an obvious absorption of g-C_3N_4 NSs and B-MoS_2@g-C_3N_4 composites is observed, and the absorption edge is *ca.* 430 nm. The band gap energy (E_g) of pure g-C_3N_4 NSs is obtained through the formula $(\alpha h\nu)^{1/2} \propto h\nu - E_g$, and the E_g of pure g-C_3N_4 NSs is calculated and the value is 2.61 eV (Fig. S4 in Supporting information). Significantly, the optical absorption of B-MoS_2@g-C_3N_4 composites is stronger than that of pure g-C_3N_4 NSs, which indicates that B-MoS_2 NSs loading onto g-C_3N_4 NSs can effectively enhance the light absorption ability of the catalyst. Among these, the light absorption of B-MoS_2@g-C_3N_4–15 composites is the strongest, which can boost the production of photogenerated carriers. To further research the role of B ions doping, the UV–vis DRS absorption spectra of MoS_2@g-C_3N_4–15 and B-MoS_2@g-C_3N_4–15 composites are shown in Fig. 3b. After B ions are doped in 1T-MoS_2 NSs, the light absorption of B-MoS_2@g-C_3N_4–15 composites is improved (yellow curve in Fig. 3b), indicating that doping B into MoS_2 can boost the utilization of light.

To study the photogenerated charge separation and transfer properties of pure g-C_3N_4 NSs, MoS_2@g-C_3N_4–15 and B-MoS_2@g-C_3N_4–15 composites, the photoelectrochemical (PEC) analysis is performed (Figs. 3c and d). Fig. 3c displays that pure g-C_3N_4 NSs, MoS_2@g-C_3N_4–15 and B-MoS_2@g-C_3N_4–15 composites present the photocurrent responses on each illumination [6]. In addition, the photocurrent values of MoS_2@g-C_3N_4–15 and B-MoS_2@g-C_3N_4–15 composites are higher than that of pure g-C_3N_4 NSs, which indicates that 1T-MoS_2 assembled on the g-C_3N_4 NSs can effectively improve the generation and separation of photogenerated carriers. Notably, the photocurrent value of B-MoS_2@g-C_3N_4–15 composites is superior to MoS_2@g-C_3N_4–15 composites, indicating that B ions doping could inhibit the recombination of electron-hole pairs. The charge transfer activity of pure g-C_3N_4 NSs, MoS_2@g-C_3N_4–15 and B-MoS_2@g-C_3N_4–15 composites is further explored through EIS measurement (Fig. 3d). MoS_2@g-C_3N_4–15 and B-MoS_2@g-C_3N_4–15 composites present a smaller arc radius than that of pure g-C_3N_4 NSs, indicating 1T-MoS_2 can accelerate carrier separation (Fig. 3d). Besides, B-MoS_2@g-C_3N_4–15 composites display the smallest arc radius, indicating the separation of photoexcited carriers of B-MoS_2@g-C_3N_4–15 composites is most effective. Hence, B ions doped into 1T-MoS_2 and MoS_2 NSs assembled on the g-C_3N_4 NSs can synergistically promote photocatalytic activity.

To explore the possibility of hydrogen production, Mott-Schottky plots are tested to estimate the conduction band (CB) potential of pure g-C_3N_4 NSs. As shown in Fig. S5 (Supporting information), g-C_3N_4 is identified as an n-type semiconductor because of the positive slope of the curves in the Mott-Schottky plots. Through extrapolation to the x-intercept in Mott-Schottky plots, the flat band potential (E_{FB}) of g-C_3N_4 is obtained (-0.42 eV *vs.* Ag/AgCl). The obtained E_{FB} is converted to a potential *vs.* standard hydrogen electrode (NHE), and then the value is subtracted by 0.2 eV to obtain an E_{CB} *vs.* NHE of the sample. Therefore, the E_{CB} of g-C_3N_4 is -0.4 eV *vs.* NHE. By the valence band potential (E_{VB}) = $E_g + E_{CB}$ and E_g results (Fig. S4 in Supporting information), the E_{VB} of g-C_3N_4 is 2.21 eV *vs.* NHE (Fig. S6 in Supporting information). Based on the above research, the E_{CB} of as-prepared g-C_3N_4 NSs is lower than 0 eV, which indicates that prepared g-C_3N_4 NSs can conduct photocatalytic hydrogen production.

Fig. 3e indicates that the photocatalytic hydrogen production of all photocatalysts is linear with time, indicating that the catalyst has stable photocatalytic H_2 evolution performance. As shown in Fig. 3f, bare g-C_3N_4 shows an unacceptable photocatalytic hydrogen evolution performance (30.82 μmol h^{-1} g^{-1}), which is attributed to the fast recombination of carriers and low light utilization. Yet, B-MoS_2@g-C_3N_4–15 composites present excellent photocatalytic hydrogen production and H_2 evolution rate, indicating that adding B-MoS_2 NSs as cocatalysts can promote the photocatalytic activity of catalysts. The H_2 evolution rate of B-MoS_2@g-C_3N_4–15 composites (1612.75 μmol h^{-1} g^{-1}) is 52.33, 1.3, 1.15 and 1.31 times of bare g-C_3N_4 NSs (30.82 μmol h^{-1} g^{-1}), B-MoS_2@g-C_3N_4–5 (1236.04 μmol h^{-1} g^{-1}), B-MoS_2@g-C_3N_4–10 (1405.12 μmol h^{-1} g^{-1}), B-MoS_2@g-C_3N_4–20 composites (1238.47 μmol h^{-1} g^{-1}), respectively. The improved photocatalytic HER performance of B-MoS_2@g-C_3N_4 composites indicates that B-MoS_2 cocatalyst loading onto g-C_3N_4 improves the utilization of light to stimulate more photogenerated electrons, accelerates carrier separation, and inhibits electron-hole pairs recombination. However, increasing B-MoS_2 NSs content from 15% to 20%, a decrease in photocatalytic performance is detected, owing to the overmuch B-MoS_2 NSs loading on g-C_3N_4 NSs impediment the photo-absorption of g-C_3N_4 NSs. As shown in Fig. S7 (Supporting information), the photocurrent values of B-MoS_2@g-C_3N_4–15 composites is higher than that of B-MoS_2@g-C_3N_4–20 composites, which indicates that the overmuch B-MoS_2 NSs loading on g-C_3N_4 NSs in B-MoS_2@g-C_3N_4–20 is adverse for the photocatalytic performance of photocatalyst. To study the effect of B ions doping, we measure the hydrogen production of MoS_2@g-C_3N_4–15 composites. As shown in Fig. S8 (Supporting information), the photocatalytic hydrogen production amount and rate of B-MoS_2@g-C_3N_4–15 composites (1612.75 μmol h^{-1} g^{-1}) is higher than that of MoS_2@g-C_3N_4–15 composites (1370.68 μmol h^{-1} g^{-1}), attributing that B ions doping into MoS_2 can activate the base planes of MoS_2 and offer more active sites. To further evaluate the H_2 production cycle property of B-MoS_2@g-C_3N_4–15 composites, the photocatalytic H_2 evolution performance is tested for 15 h (Fig. S9 in Supporting information). Almost 92.4% of the incipient property is kept, and the micromorphology of B-MoS_2@g-C_3N_4–15 composites after the cycle test (Fig. S10 in Supporting information) does not change

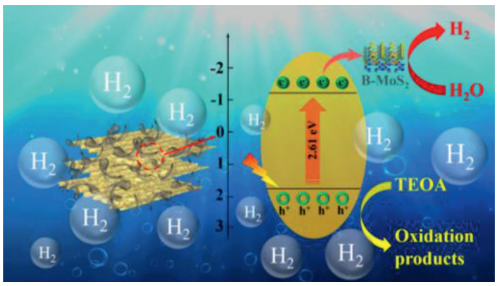

Scheme 1. Schematic illustration of the photocatalytic H_2 evolution mechanism of B-MoS_2@g-C_3N_4 composites.

significantly, indicating the good stability of B-MoS_2@g-C_3N_4–15 composites. We further determine the apparent quantum efficiency (AQE) of pure g-C_3N_4 NSs and B-MoS_2@g-C_3N_4–15 composites under light at $\lambda = 370$ nm irradiation. As shown in Fig. S11 (Supporting information), the AQE value of B-MoS_2@g-C_3N_4–15 composites (5.54%) is higher than that of bare g-C_3N_4 NSs (0.41%), which illustrates the optical utilization of B-MoS_2@g-C_3N_4–15 composites is higher than that of pure g-C_3N_4 NSs.

According to the above studies, we propose a possible photocatalytic hydrogen evolution mechanism to explicate the reason for the improved photocatalytic hydrogen evolution performance of B-MoS_2@g-C_3N_4 composites (Scheme 1). The loading of B-MoS_2 NSs improves the light absorption of g-C_3N_4 to stimulate more photogenerated carriers and offer more active sites for HER. In addition, B-MoS_2 as a cocatalyst can capture photoinduced electrons, accelerate electron transfer and inhibit recombination of electron-hole pairs. B ions are doped into the lattice of 1T-MoS_2, which can activate more base planes of 1T-MoS_2 and is suitable for the HER to activate H^+. The photoexcited electrons produced under the sunlight through g-C_3N_4 moved to B-MoS_2, and then reduced water to hydrogen. Concurrently, TEOA as a sacrificial agent consumed the holes. Hence, the close combination of B-MoS_2 and g-C_3N_4 boosts the photocatalytic hydrogen evolution activity of photocatalysts.

In conclusion, we have successfully synthesized an efficient B-MoS_2@g-C_3N_4 composite for photocatalytic H_2 evolution *via* cocatalyst and doping strategy. The as-prepared B-MoS_2@g-C_3N_4 composites with 15 wt% B-MoS_2 (B-MoS_2@g-C_3N_4–15) present an extremely improved photocatalytic H_2 evolution rate of 1612.75 μmol h^{-1} g^{-1}, which is 52.33 times of bare g-C_3N_4 NSs (30.82 μmol h^{-1} g^{-1}). The above experimental results confirm that the enhanced photocatalytic activity of B-MoS_2@g-C_3N_4–15 composites may be assigned to the following factors: (1) As a cocatalyst, B doped 1T phase MoS_2 NSs greatly improves the light utilization of photocatalyst and stimulates more photogenerated carriers; (2) B-MoS_2 NSs with excellent conductivity are closely connected onto g-C_3N_4 NSs, which can accelerate electron transfer and inhibit carrier recombination; (3) The base planes are activated through doping B ions into the lattice of MoS_2, which can induce the distortion of MoS_2 crystal and provide more active sites for HER. This easy assembly strategy offers guidance for rationally constructed photocatalysts based on B-doped 1T phase MoS_2 as a cocatalyst for H_2 production.

Declaration of competing interest

The authors declare that they have no known competing financial interests or personal relationships that could have appeared to influence the work reported in this paper.

Acknowledgments

The authors are thankful for fundings from the National Natural Science Foundation of China (No. 51872173), Taishan Scholars Program of Shandong Province (No. tsqn201812068), Natural Science Foundation of Shandong Province (No. ZR2022JQ21), and Higher School Youth Innovation Team of Shandong Province (No. 2019KJA013). The authors would like to thank Shiyanjia Lab (www.Shiyanjia. Com) for the XPS analysis.

Supplementary materials

Supplementary material associated with this article can be found, in the online version, at doi:10.1016/j.cclet.2023.108246.

References

[1] Y. Zhang, Z. Huang, Y. Dong, et al., Chem. Eng. J. 431 (2022) 134101.
[2] X. Wang, J. Gong, Y. Dong, et al., Mater. Today Phys. 27 (2022) 100806.
[3] W. Zhao, H. Niu, Y. Yang, et al., J. Environ. Sci. 2 (2022) 14.
[4] P. Qiu, R. Hu, X. Wang, et al., Mater. Chem. Front. 6 (2022) 718.
[5] J. Huang, J. Mei, J. Han, et al., J. Colloid Interface Sci. 556 (2019) 224–231.
[6] Z. Zhang, Y. Xue, X. Wang, et al., Chem. Eng. J. 421 (2021) 130016.
[7] J. Fu, Q. Xu, J. Low, et al., Appl. Catal. B: Environ. 243 (2019) 556–565.
[8] Q. Gong, S. Cao, Y. Zhou, et al., Int. J. Hydrog. Energy 46 (2021) 21442–21453.
[9] Y. Li, S. Zhu, X. Kong, et al., Environ. Res. 197 (2021) 111002.
[10] Y. Zhou, Y. Zhang, J. Xue, et al., Chem. Eng. J. 420 (2021) 129574.
[11] H. Zhou, R. Chen, C. Han, et al., J. Colloid Interface Sci. 197 (2021) 111002.
[12] W. Qureshi, X. Hong, X. He, et al., Chemosphere 291 (2022) 132987.
[13] L. Wang, Y. Qi, H. Li, et al., Sci. China Mater. 65 (2022) 974–984.
[14] B. Sun, P. Qiu, Z. Liang, et al., Chem. Eng. J. 406 (2021) 127177.
[15] Z. Liang, Y. Xue, X. Wang, et al., Mater. Today Nano 18 (2022) 100204.
[16] C. Sun, L. Wang, W. Zhao, et al., Adv. Funct. Mater. 32 (2022) 2206163.
[17] H. Zhao, Z. Jiang, K. Xiao, et al., Appl. Catal. B: Environ. 280 (2020) 119456.
[18] H. Yuan, F. Fang, J. Dong, et al., Colloid. Surfaces A 641 (2022) 128575.
[19] C. Vennapoosa, S. Gonuguntla, S. Saddam, et al., ACS Appl. Nano Mater. 5 (2022) 4848–4859.
[20] X. Chen, S. Zhang, X. Qian, et al., Appl. Catal. B: Environ. 310 (2022) 121277.
[21] X. Chen, C. Ma, Z. Tan, et al., Chem. Eng. J. 433 (2022) 134504.
[22] H. Xu, J. Yi, X. She, et al., Appl. Catal. B: Environ. 220 (2018) 379–385.
[23] Y. Jia, Z. Wang, L. Wang, et al., ChemSusChem 12 (2019) 3336–3342.
[24] M. Liu, H. Li, S. Liu, et al., Nano. Res. 15 (2022) 5946–5952.
[25] X. Cheng, L. Wang, L. Xie, et al., Chem. Eng. J. 439 (2022) 135757.
[26] J. Deng, H. Li, J. Xiao, et al., Energy Environ. Sci. 8 (2015) 1594–1601.
[27] P. Qiu, Z. Liang, X. Liu, et al., J. Colloid Interface Sci. 571 (2020) 318–325.
[28] X. Zhang, S. He, S. Jiang, Carbon 156 (2020) 488–498.
[29] J. Sun, S. Yang, Z. Liang, et al., J. Colloid Interface Sci. 567 (2020) 300–307.
[30] Y. Chang, Z. Liu, X. Shen, et al., J. Hazard. Mater. 344 (2018) 1188–1197.
[31] F. Shaik, R. Milan, L. Amirav, ACS Appl. Mater. Interfaces 14 (2022) 21340–21347.
[32] X. Wang, Y. Xue, Z. Liang, et al., Mater. Today Adv. 15 (2022) 100257.
[33] D. Wei, Y. Liu, X. Shao, et al., J. Environ. Chem. Eng. 10 (2022) 107216.
[34] Q. Liu, Q. Fang, W. Chu, et al., Chem. Mater. 29 (2017) 4738–4744.
[35] X. Li, X. Lv, N. Li, et al., Appl. Catal. B: Environ. 243 (2019) 76–85.